Volume 1 | Number 1 | Jan 2013 | Pages 1–100

Journal of
Materials Chemistry A

Materials for energy and sustainability
www.rsc.org/materialsA

ROYAL SOCIETY OF CHEMISTRY

www.rsc.org/materialsA

TOC
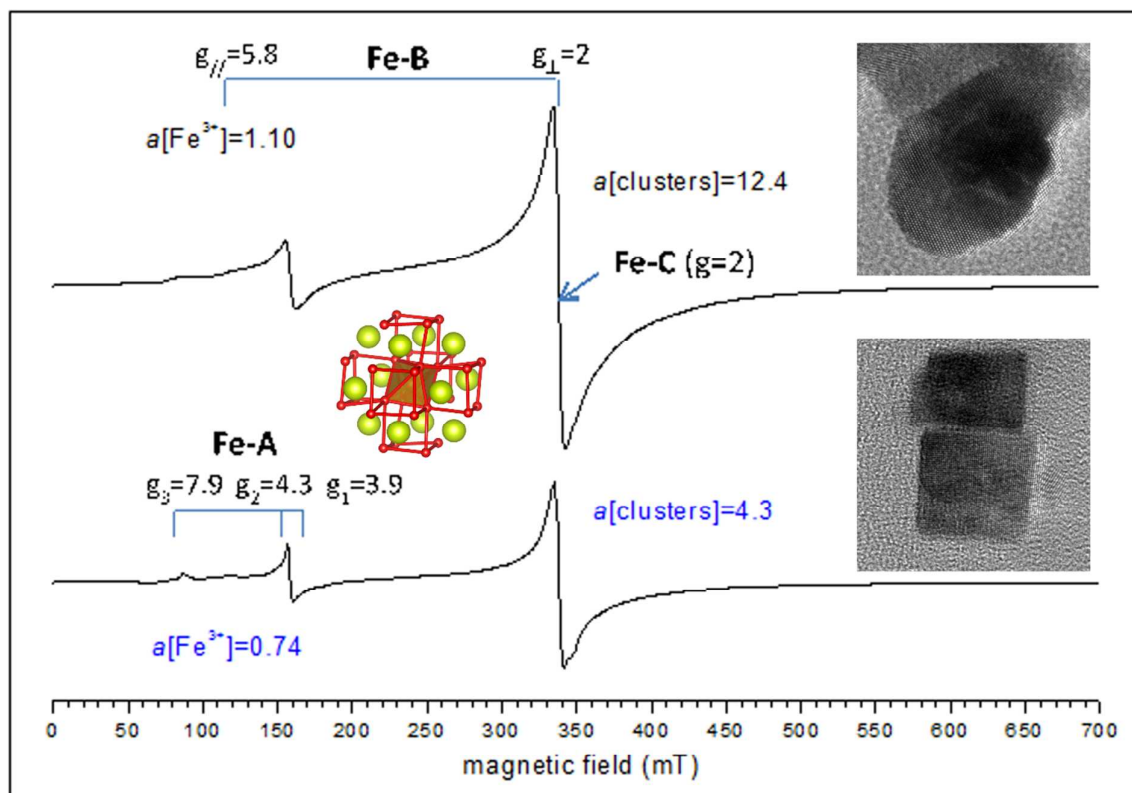
Local organization of Fe^{3+} into nano-CeO_2 with controlled morphologies and impact on reducibility properties

Iona Moog[1], Cédric Feral-Martin[1], Mathieu Duttine[1], Alain Wattiaux[1], Carmelo Prestipino[2], Santiago Figueroa[3], Jérôme Majimel[1], Alain Demourgues[1*]

1. CNRS, University of Bordeaux, ICMCB, UPR 9048, F-33600 Pessac, France
2. Sciences chimiques de Rennes, UMR-CNRS 6226. Campus de Beaulieu, Bat 10B. 35042 Rennes. France
3. European Synchrotron Radiation Facility, 6, rue Jules HOROWITZ, BP220. 38043 Grenoble. France

*: corresponding author

Abstract

Ce and Fe are the main metal additives which have been tested by many laboratories for their catalytic activity at low temperature for soot oxidation in diesel engines. Then, the key role and impact of Fe on the reducibility properties of ceria have been investigated on the basis of the composition and the structural features considering various synthesis routes. Two different procedures were used to prepare iron-substituted cerium dioxide $Ce_{1-x}Fe_xO_{2-x/2}$: a classical co-precipitation route followed by annealing at T=600°C and an unusual microwave-assisted hydrothermal synthesis at T=200°C. The highest surface areas around 100 m^2/g, have been obtained for oxides containing the largest Fe amount and prepared by microwave-assisted route. Solid solutions were obtained up to x=0.15 and 0.20 for microwave-assisted and co-precipitation routes respectively. The highest decrease of the lattice parameter is observed for compounds prepared by microwave-assisted route. The TEM analysis reveals a nano-cubic shape (with mainly {001} planes) for compounds prepared by microwave-assisted route and containing low Fe amount. For the other compounds prepared also by co-precipitation process, a nano-polyhedron shape corresponding to the thermodynamically stable morphology, is observed. EPR (T=5K, very low Fe rates), Mössbauer (Room Temperature, x=0.10) and XANES-EXAFS (RT and T=20K) spectroscopies studies showed that Fe ions adopt the trivalent state and are located in isolated distorted (orthorhombic and axial distortions) octahedra or form Fe clusters. The local organization of Fe^{3+} plays a key role in the oxygen vacancy distribution and consequently to the reducibility properties of the $Ce_{1-x}Fe_xO_{2-x/2}$ solid solution. For the compounds prepared by microwave-assisted route, a large proportion of Fe^{3+} is located in isolated distorted octahedral sites contributing to affect a

high number of Ce^{4+} nearest neighbors with a high mobility of oxygen vacancies. In this case, the oxygen vacancies are well distributed around Ce^{4+} and Fe^{3+}. In the case of compounds obtained by co-precipitation route, Fe clusters abundance is higher and consequently oxygen vacancies are mainly located around Fe clusters. Such a distribution should explain the lower solubility limit and the larger variation of the cell parameter versus x Fe content in the series prepared by microwave-assisted route. It is shown that these last compounds exhibit better reducibility properties with a doubled reduction rate (comparison between x(Fe)=0.05 and pure CeO_2) equal to 60% at T=550°C due to the iron local organization, a nano-cubic morphology and a higher surface area.

Introduction

Numerous works have been devoted to ceria and related materials used as oxygen buffers in catalysts for removing hydrocarbons, carbon monoxide and nitrogen oxides from automobile exhausts [1-2]. The creation of anionic vacancies into the fluorite-type networks are associated to the valence change of Ce between $Ce^{4+}(4f^0)$ and $Ce^{3+}(4f^1)$. The rate of reduced cerium ions stabilized into the structure must be large and the reduction has to occur at low temperature. There are several driving concepts to increase the Ce reducibility or Ce^{3+} stabilization at low temperatures into the fluorite-type structures. The formation of high content of Ce^{3+} at low temperature is possible when Ce^{4+} polyhedra are locally distorted, creating mainly $Ce^{4+}-O^{2-}$ ionic bonds. Then, creation of oxygen vacancies and consequently oxygen diffusion become easier.

By playing with the structural features, the local environment of Ce can be modify by appropriate cations substitutions [3] such as Zr^{4+} [4,5] or lanthanides Ln^{3+} [6-12] and lead to various crystallized networks and space groups related to the fluorite-type structure such as tetragonal fluorite (SG : $P4_2/nmc$) [13], Pyrochlore (SG: Fd-3m) [5] or Bixbyite (SG : Ia-3) [14]. Furthermore appropriate cations substitutions without structural change by keeping the fluorite network, allow modifying the redox properties [3]. The competitive bonds around Ce^{4+} will play indeed a key role in this latter case.

Finally high surface areas and various morphologies exposing various Ce/O reticular planes with different local environments, charges [15] and atomic density allow reaching high reduced Ce rates at low temperatures. Theoretical calculations [16] have shown that the formation energy of anion vacancies for various CeO_2 surface follows the order {110} < {100} < {111}. Hydrolysis of cerium salts combined with hydrothermal treatment allows preparing single crystalline CeO_2 nano-polyhedra revealing {111} and {100} planes, nanocubes with {100} planes and nanorods with {111} and {001} planes

[15]. Then, because of theses shapes and revealed reticular planes, the ability to release oxygen and the reducibility will change for the various geometries.

Hydrolysis and precipitation of Ce^{3+} salt in basic medium followed by annealing at high temperatures [17, 18], sol-gel methods [19] and hydrothermal routes [4, 20] are the common processes to prepare high surface areas CeO_2. Other rare earths metals or transition metals substituting $Ce^{4+}$are directly incorporated into the solutions containing different salts. The pH can be adjust depending on the precipitation domain.

Most of rare earth ions, for instance from La^{3+} to Tb^{4+} [6-12] have been substituted for Ce^{4+} and anionic vacancies are stabilized into the fluorite network as trivalent rare earth ions are incorporated. The largest increase of the cell parameter is observed when La^{3+} [6-7] are substituted for Ce^{4+} despite the creation of oxygen vacancies. The cell parameter expansion decreases when Gd^{3+} ions [11] are incorporated in the fluorite network and it remains constant as Pr^{4+} or Tb^{4+} [7,12] are present. The ionic radius of rare earths governs the variation of the cell parameter. For other tetravalent cations such as Zr^{4+} [21] or Sn^{4+}[22], derived structures from fluorite-type network can be stabilized and the Ce reducibility is enhanced thanks to a change of the local environment of Ce^{4+}.

For transition metals, substitution of Ce^{4+} ions and insertion into vacant sites of fluorite network can be considered. However, except for Zr^{4+} as well as Sn^{4+} ions whose the ionic size is smaller than that of Ce^{4+} but higher than that of others 1st row transition metals, it is often very difficult to conclude about the solubility limit and the variation of the cell parameter. In the case of Ti^{4+} where an enhancement of reducibility properties has to be also noted [23, 24], the cell parameter slightly decreased (from 5.41 to 5.39 Å) as a high content of Ti^{4+} equal to 40% is reached. EXⵁFS study reveals the occurrence of a (4+4) local environment of Ti^{4+} with Ti-O bond distances at 1.9 Å and 2.5 Å respectively [24]. In the case of trivalent [25-26] or divalent transition metals [27] substituted for Ce^{4+}, oxygen vacancies are stabilized due to charge electroneutrality.

To improve the oxidation rate of a diesel particulate matter at low temperatures, a combination of a particulate filter and a metal fuel additive is used today in most of vehicles. Ce and Fe are the main metal additives which have been tested for their activity at low temperature for soot oxidation during the last 20 years. For Fe^{3+}ions, numerous works mention the occurrence of substitution as well as insertion sites with distorted octahedral sites [17-20, 28-34]. Then the existence of defects $3Fe'_{Ce}:Fe_i^{\cdot\cdot}$ (in the Kröger–

Vink notation) has been proposed [35] to explain the absence of oxygen vacancies revealed by the Raman study. If Fe^{3+} ions are incorporated in the cationic holes of the fluorite network, strong Ce-Fe interactions at around 2.7 Å appear and because of the reorganization of oxygen and vacancies, the occurrence of Fe insertion into fluorite is highly improbable whereas Fe substitution for Ce^{4+} seems more evident. The highest Fe rate around 0.3 [36] has been stabilized into ceria and the cell parameter can decrease from 5.41 to 5.34 Å. Moreover, the Fe content and its oxidation state as well the variation of the cell parameter strongly depend on the synthesis route [17-20, 28-36]. Some authors mention indeed the stabilization of Fe^{2+}/Fe^{3+}valence states in doped-CeO_2 nanocrystals as well as the occurrence of oxygen vacancies revealed by Raman spectroscopy [37-38]. Then, many controversies exist about the local environment of Fe^{3+} into ceria as well as the variations of cell parameter and the solubility limit. Finally the relationships between composition, structural features and Ce reducibility must be explained.

This paper aims to investigate the structural features of $Ce_{1-x}Fe_xO_{2-x/2}$ solid solutions and the impact on reducibility properties. Two different routes, the co-precipitation method (CP) followed by annealing at T=600°C and microwave-assisted process (MW) were used to obtain the $Ce_{1-x}Fe_xO_{2-x/2}$ solid solution. Microwave-assisted synthesis is an interesting route because of the short reaction time, the homogeneous temperature [39] and the absence of further heat treatment. It is interesting to compare both these synthesis routes, because the kinetics of reactions and the way to incorporate Fe into ceria are clearly different. Furthermore the morphologies of the nanoparticles as well as the surface areas will not be the same.

In this study, structural characterizations have been carried out on as-prepared pure compounds. Mössbauer, EPR and X⬛NES-EX⬛FS spectroscopies are used to probe iron local environment and its oxidation state. The variations of the cell parameter and the solubility limit have been determined from Le-Bail refinement of XRD data. TEM analysis allowed identifying the various shapes of single nano-crystalline $Ce_{1-x}Fe_xO_{2-x/2}$. Finally, as a function of the synthesis routes, TG⬛ measurements under ⬛r/5% H_2 of $Ce_{1-x}Fe_xO_{2-x/2}$ oxides have been undertaken in order to evaluate the reducibility properties which have been correlated to the structural features.

Experimental section

(a) Synthesis

(i) Preparation of the $Ce_{1-x}Fe_xO_{2-x/2}$ mixed oxides by co-precipitation (CP) in basic medium. The solid solution was prepared for x = 0, 0.05, 0.1, 0.15 and 0.25. Cerium nitrate hexahydrated $Ce(NO_3)_3 \cdot 6H_2O$ (Rhodia chemicals, 99,9%) and iron nitrate nonahydrated $Fe(NO_3)_3 \cdot 9H_2O$ (Sigma Aldrich, 99,99%) were used as precursors. Stoechiometric proportions of solutions were precipitated under vigorous stirring into ammonia 0,1M. While adding the acid precursor solution, the pH was maintained at a value close to 10 using concentrated NH_4OH (12,3M) and then left under stirring for 2 hours. The precipitated oxides or oxy-hydroxides were then washed and centrifuged three times (5000 rpm) with 100 ml distilled water. It was then dried overnight in an oven at 100 °C and finally annealed for 5 hours at 600 °C.

(ii) Preparation of the $Ce_{1-x}Fe_xO_{2-x/2}$ mixed oxides using a microwave-assisted (MW) route. The solid solution was prepared for x = 0, 0.05, 0.1, 0.15 and 0.17. The same precursors (around 20 ml for the precursors solution) were used and were precipitated in a highly basic medium composed of sodium hydroxide (around 25 ml for the NaOH solution, 35% weight) and ammonia (around 3 ml for the NH_4OH solution, 25% weight) with a $n_{base}/n_{cations}$ molar ratio equal to 175. The molar ratio $[NaOH]/[NH_4OH]$ was equal to 1.8. The solution (40-50 ml) containing precipitated oxides and oxy-hydroxides was then incorporated into a closed Teflon vessel (120 ml), heated up to 200°C for 40 min using the microwave system (CEM, MARS) operating at 2450 MHz and then cooled at room temperature. A self-generating pressure of 20 bars was induced by the increase of temperature inside the Teflon container. The precipitate so obtained was finally centrifuged at 5000 rpm and washed three times with 100 ml of distilled water and dried overnight.

In a first step, the process of hydrolysis, oxidation and nucleation in basic medium of $Ce(OH)_3$ occur in CP and MW syntheses and involves the formation of complexes with water and hydroxyls molecules such as $[Ce(OH)_x(H_2O)_y]^{(4-x)+}$ where x+y is the coordination number of Ce^{4+}. In a second step, condensation processes take place with the formation of $CeO_2 \cdot nH_2O$. This latter stage differs greatly depending on the chosen synthesis.

The microwave-assisted route leads to fast and homogenous nucleation due to the important interactions between the molecules where ionic and dipolar polarizations contribute to heating. Then, heating at the core of the polar molecules, leads to the formation of nanocrystalline $Ce_{1-x}Fe_xO_{2-x/2}$ with defined shapes. In the case of the classical coprecipitation route further annealing at 600°C have been performed in order to eliminate residual nitrates. Only, the thermodynamically stable form corresponding to polyhedral nanocrystals have been obtained after CP synthesis and annealing at T=600°C.

Cations ratio were checked for both synthesis with the ICP-OES (Inductively Coupled Plasma Spectroscopy) technique and found to be in the right chemical composition. The samples have been firstly dissolved using hydrochloric acid and heated at T=200°C during 15 min using microwave digestion system (CEM, M RS).

(b) XRD and X FS experiments. Powder X-ray diffraction patterns were recorded on a P Nalytical X'Pert MPD apparatus equipped with a Ge(111) Cu Kα monochromator (λ=1.54059 Å) and an X'Celerator detector. Data were collected over a range of 10°-110° with 0.017° steps. The lattice parameters and the crystallite sizes were determined by profile matching (Le-Bail fit) using the Thomson-Cox-Hastings function implemented in the Fullprof program package [40]. X-ray absorption experiments (X NES and EX FS) at the Fe K-edge (7112 eV) were carried out for compounds obtained by the microwave-assisted route. Data were collected at room temperature on station BM23 (upgrade of BM29 [41]) at ESRF-Grenoble-France in uniform filling Operation Modes. The beam was monochromatized by a Si (111) double crystal monochromator and harmonics rejection was assured by a Si double mirror. Spectra were recorded in fluorescence mode using a 13 monolithic Ge elements detector mode.

Further experiment collected at T=20K with a helium cryostat have been performed on SAMBA beamline [42] at SOLEIL-Saclay-France. The beamline is equipped by a sagittal focusing Si(111) monochromator and a 13 monolithic Ge elements detector. EXAFS spectra at the Fe K-edge (7112 eV) were reduced to normalized XAFS $\chi(k)$ using Ifeffit software [43].

Least squares analysis against model environment were calculated and compared with hematite α-Fe_2O_3 and maghemite γ-Fe_2O_3. Only the first shell can be refined and lead to the determination of 3 parameters, the radial Fe-O bond distance, the $2\sigma^2$ Debye-Waller

factor and the zero energy shift. As far as the second shells are concerned and especially the Fe-Ce interactions, it is impossible to conclude about the occurrence of such local environments because of the too low signal/noise ratio. The results have been compared with XRD analysis and have been reported on Table 3.

(c) BET measurements. Surface areas were determined using the Brunauer, Emmet and Teller (BET) calculations on isotherms recorded with an Autosorb-1 from Quantochrome Instrument apparatus. Outgassing temperatures were set to 150°C for MW samples and 300°C for CP ones.

(d) EPR and Mössbauer measurements. Electron paramagnetic resonance spectra were recorded at T = 5 K with a Bruker EMX spectrometer at X-band frequency (9.45 GHz) in order to identify the Fe^{3+} local environments. The WinEPR and SIMFONIA program were used to simulate and quantify the detected EPR spectra.

Mössbauer measurements were performed with a constant acceleration Halder – type spectrometer using a room temperature ^{57}Co source (Rh matrix) in the transmission geometry. The polycrystalline absorbers containing about $10mg/cm^2$ of iron were used to avoid the experimental widening of the peaks. The velocity was calibrated using pure iron metal as the standard material.

At 293 K, a preliminary refinement using Lorentzien profile lines shown that the spectrum consists of two doublets assigned to two sites of Fe^{3+}. Nevertheless, the large values of the line width implied the existence of distributions of quadrupole splitting. Thus, a second calculation using quadrupole splitting distributions has been realized. For that, the value of the half height width was fixed at 0.30 mm/s and the isomer shift values are those determined from the first calculation.

(e) TGA analyses. Thermogravimetric analyses (TGA) were carried out in a controlled reducing atmosphere composed of 95% of Argon and 5% of H_2 on a Seteram thermal analyzer. The weight losses versus temperature were recorded at 5°C/min heating rate from room temperature to 700°C. One should have to notice that pure ceria prepared by MW route exhibit a higher surface area than ceria obtained by CP-process and consequently various molecules such as H_2O and CO_2 for instance, can be adsorbed in large quantities at T<300°C-350°C (identified by TGA coupled with FTIR and mass spectrometer).

(f) TEM pictures. To examine the size and the morphology of particles, transmission electron microscopy (TEM) pictures were recorded using a microscope JEOL 2200FS equipped with a field emission gun, operating at 200 kV with a point resolution of 0.23 nm. Few drops of the powder in ethanol suspension was placed on a carbon-copper grid and air-dried.

Results and discussion

(a) XRD and TEM analysis: cell parameter variations, solubility limits and morphologies.
All the synthesized compounds were firstly characterized by X-ray diffraction (Figure 1 A and B). The XRD patterns show the reflections characteristic of the cubic fluorite structure of CeO_2. The solid solution $Ce_{1-x}Fe_xO_{2-x/2}$ exists for values going from x = 0 to x = 0.15 and x = 0.20 for microwave-assisted route and coprecipitation synthesis respectively. Above these values, the appearance of the (110) peak characteristic of the α-hematite indicates the end of solubility of iron into the CeO_2 network. For both solid solutions obtained by various synthesis routes, a shift to the higher angles was observed as the iron concentration increases. A clear decrease of the unit cell parameter versus Fe (x) content can be noticed (Table 1). This result is in good agreement with the substitution of a smaller cation (Fe^{3+}, 0.65Å, High Spin state), 6-fold coordinated to oxygen, stabilized into ceria network with oxygen vacancies, compared to Ce^{4+} (0.97Å) which occupy a cubic environment into the fluorite-type network. Moreover, taking into account the ionic radii of Fe^{3+}, 6-fold coordinated to oxygen and the various results of the literature [17-20, 28-36], the variations of the cell parameter appear in the right range. A linear combination of 85% of Ce-O bonds with Ce^{4+} (0.97 Å), 8-fold coordinated to oxygen and 15% of Fe-O bond distances with Fe^{3+} (0.65 Å), 6-fold coordinated to oxygen, leads indeed for x=0.15 to a theoretical cell parameter around 5.36 Å close to the unit-cell parameter of the compound prepared by microwave-assisted route (x=0.15, a = 5.371 Å).

However, for the same x (Fe) content the values differ as a function of the synthesis routes (Figure 2). For instance, for x=0.15, the cell parameter is smaller and equal to 5.371 Å in the case of MW process than in the case of CP method where a = 5.389 Å. Nevertheless, for lower Fe concentrations, the CP synthesis leads to the smaller cell parameters and finally the compounds prepared by microwave-assisted route exhibit the

cell parameters which vary in the largest range. These variations should be due to the nature of Fe ions substituted for Ce^{4+} one's and will be discussed in the followings paragraphs.

 broadening of the peaks is also noticed as the iron concentration increases and is associated to the decrease of the crystallite sizes. In order to calculate accurate values for the microstrains and the crystallite size, the peak profiles are fitted using the pseudo-Voigt function of Thompson-Cox-Hastings [44] which allows refining separately the angular dependence of both Lorentzain (H_L) and Gaussian (H_G) components of FWHM. s already observed for other solid solutions such as $Ce_{1-x}Eu_xO_{2-\delta}$ [45] or $Ce_{1-x}Ca_xO_{2-\delta}$ [46], the substitution of trivalent or divalent cations leads to a global decrease of the crystallites size or coherent domains due to the creation of constraints and oxygen vacancies into the network and the competition between surface and Madelung energies which limit the crystal growth [47, 48]. The average size of the nanoparticles determined on the basis of XRD data refinements (Table 1) decreases from a size of about 20 nm (x=0) to 10 nm (x=0.15) for both synthesis routes. The surface areas were determined using BET measurements (Table 1). For the MW compounds the surface areas variation is in good agreement with that of refined crystallite sizes on the basis of XRD data, showing an increase of the surface area with an increase of iron concentration. The values go from $40m^2.g^{-1}$ to $95m^2.g^{-1}$. In the case of CP compounds surface areas vary between 20 and $60m^2.g^{-1}$. Despite similar crystallite sizes – as shown by XRD analyses – the measured surface areas of CP and MW compounds are different. This can be due to the annealing at T=600°C of CP nanoparticles. Thermal treatment is indeed going to induce the creation of sintering necks between the particles therefore decreasing the accessible surface areas. The higher surface areas found in MW compounds is consistent with the experimental procedure with fast nucleation process, relatively short synthesis durations and the absence of annealing at higher temperatures. One should have to notice that surface areas change drastically around x=0.07 (Table 1).

The Fe solubility limit, the lattice parameter values and its variation determined for both synthesis routes cannot be explained by considering various surface areas and crystallite sizes leading to different metastable phases due to the competition between surface and Madelung energies. The lowest Fe solubility does indeed correspond to compounds prepared by MW process with the highest surface areas. Then, the local organization of

Fe and Ce cations into the fluorite network should probably explain such values and variation.

One should have to note that compounds prepared by CP-method followed by annealing at high temperatures exhibit polyhedral morphologies, revealing {111} and {001} reticular planes. In the case of MW-assisted route, a cubic morphology with mainly the {001} planes which are more active for reducibility than {111} planes, is identified for low Fe content. Furthermore, as the Fe rate increases (x>0.10), a more classical polyhedral morphology appears and the surface area increases (Figure 3).

(b) EPR, Mossbauer and X‑NES-EX‑FS spectroscopies analyses: information about the Fe^{3+} local environment.

In order to determine the iron local environments for both synthesis routes, EPR and Mössbauer spectroscopies studies were carried out. Compounds with low iron concentrations ($0.001 \leq x \leq 0.01$) were used for the EPR analyses in order to reduce the effect of dipolar interactions and thus to increase the signal resolution. Fe^{3+} among the transition metal ions belongs to the half-filled $3d^5$ electronic configuration and exhibits $^6\text{‑}_{1g}$ ground state with High Spin state (S=5/2) and quenched orbital angular momentum (L=0) under weak or intermediate crystal field. Then, the crystal field, the O-Fe charge transfer and bond covalency must affect mainly the g values determined by EPR measurements.

The g values will therefore be different according to the coordination number and the symmetry of the local site. The obtained spectra (Figure 4) can be decomposed into two parts: one centered around 350 mT for high fields and another around 50 to 250 mT and all these signals are unambiguously attributed to Fe^{3+} [35, 49, 50].

The variation of the EPR spectra between 5K and room temperature has allows to assign the spectrum features to three different iron environment, the first two corresponding to isolated Fe^{3+} (label in figure 4 Fe-‑ and Fe-B respectively) and last to cluster species (label in figure 4 Fe-C). The first site (Fe-‑) are ascribed to high g values at 3.9, 4.3 and 7.9 (g_1,g_2,g_3 respectively), corresponding to low fields region and Fe^{3+} in an isolated octahedral site with an orthorhombic distortion. This distorted octahedral environment could be associated to C_{2v} point group with 3 different Fe-O bond distances. We also observed a less intense axial signal (Fe-B) with g values $g_{//}=5.8$ and $g_{\perp} \sim 2$ which is due

to Fe^{3+} ions located in distorted octahedral sites with axial distortion [49]. In this case, the local symmetry could be D_{3h}, with six equal Fe-O bond distances.

Both these distorted octahedral sites can be identified in Bixbyite $(Fe,Mn)O_3$ [14, 51] with Ia-3 space group which derive from Fm-3m space group of the fluorite-type network. The first site is surrounded by three kinds of Fe-O bond distances, from 1.93 Å to 2.15 Å, forming a distorted octahedron with C_{2v} point group whereas for the second site six equal Fe-O bond distances at around 2.0 Å associated to a flattened octahedral site correspond to the D_{3h} symmetry [51].

 In addition to these two signals associated with isolated Fe^{3+} ions in distorted octahedral sites, a broad (about 10 mT) and intense line was observed at g~2 (signal C). This last signal may be attributed to clusters of Fe^{3+} coupled with strong spin-spin interactions [52]. Its position and width which mainly depend on dipole-dipole and exchange interactions remain unchanged as temperature decreases and whatever Fe concentration is ($0.001 \leq x \leq 0.01$) whereas its intensity increases with x Fe content. Thus the size of Fe clusters remains the same but its amount increases with Fe concentration (Figure 5). $a(Fe^{3+})$ values represent the normalized areas under the two main regions at low (g=7.9-3.9) and high fields (g=2). The different a values (Figures 4a-b) associated to isolated Fe^{3+} in octahedral coordination or to Fe^{3+} clusters lead to conclude that the relative concentration of clusters is higher in the case of CP compounds compared to MW ones. These Fe^{3+} clusters are localized into ceria network on the basis of Fe K-edge X NES analysis presented in the following section. (see below).

It should be noticed that EPR spectra show, even at room temperature, a weak axial signal D (figure 5) with g values $g_{\perp}=1.964$ and $g_{//}=1.942$. The assignment of this signal, which was observed in many ceria-containing materials, remains unclear. It has been assigned to either unpaired electrons trapped at oxygen vacancies (stabilized by impurities or structural defects) or delocalized among ions in the direct vicinity of these vacancies [53] or Ce^{3+} ions in low symmetry sites within the CeO_2 network [54]. However, 4f electrons associated to rare earths and Ce^{3+} can be detected by EPR only at T<20K because of their short relaxation times. In this case, local magnetic interactions with Fe^{3+} ions and high distortions of Ce^{3+} sites would lead to increase the relaxation time and then allows the detection of Ce^{3+} EPR signal even at room temperature. Furthermore, the concentration of Ce^{3+} paramagnetic species does remain low in these samples and does not affect the reducibility properties [53, 54]

For low Fe^{3+} content, EPR analyses show that the local organization of Fe^{3+} is strongly dependent on the synthesis routes. In order to confirm such tendency for higher Fe^{3+} concentrations, Mössbauer spectroscopy investigations have been performed.

Mössbauer spectroscopy analyses were carried out on $Ce_{0.9}Fe_{0.1}O_{1.95}$ compounds synthesized using both procedures (Figure 6). No trace of magnetic α-Fe_2O_3 was found on the basis of Mössbauer spectroscopy experiments performed at high velocities with a detection limit lower than 1% but this cannot rule out the occurrence of small α-Fe_2O_3 clusters. For both the samples, the Mössbauer spectra, recorded at room temperature reveal two octahedral Fe^{3+} components where the proportion depends on the synthesis route (Table 2). The isomer shifts δ vary between 0.30 and 0.38 mm/s with two extreme values around 0.30 and 0.38 mm/s associated to the two components with various distribution of quadrupole splitting. The higher the isomer shift, the more ionic the chemical bonding. Then, the lowest isomer shifts could be associated to the most covalent Fe-O bonding mainly attributed to Fe^{3+} clusters. The other component with an isomer shift around 0.38 mm/s could be mostly affected to isolated Fe^{3+} octahedral sites. Moreover the average quadrupole splitting Δ based on a distribution of quadrupole splitting is slightly higher for the first site and consequently related to a more distorted octahedral site. Taking into account the various values of the isomer shifts and quadrupole splittings as well as the content of each component, it is then possible to assign these signals. The first site correspond to Fe^{3+} in clusters with a more covalent Fe-O bonds and stronger distortions while the second site is mainly associated to isolated Fe^{3+} with more ionic Fe-O bonds where the site distortion is less pronounced. Finally, because of these values and the distribution of each component, compounds prepared by CP-route seem to exhibit a higher content of Fe^{3+} clusters in good agreement with EPR measurements performed on samples with low Fe^{3+} content.

The Fe-K edge X-NES spectra (recorded at room temperature) of the $Ce_{1-x}Fe_xO_{2-x/2}$ solid solution with x = 0.05, 0.1, 0.15 and 0.17 prepared by MW-assisted route are shown on Figure 7. The Fe K-edge X-NES spectra and Fourier Transforms of EX-FS oscillations (recorded at T=20K) of $Ce_{0.9}Fe_{0.1}O_{1.95}$ oxides prepared by CP or MW-assisted routes have been compared with α-hematite Fe_2O_3 on Figures 8a-b. Fe K-edge X-S data acquisition at

T=20K allows limiting the atomic thermal displacements and the Debye-Waller factors. The Fe K-edge X⬚NES spectra can generally be split into two regions. ⬚ pre-edge consisting of low intensity Fe 1s → 3d quadrupole transitions appear between 7110 and 7120 eV which are actually partially dipole allowed transitions due to 3d-4p mixing of the Fe^{3+} and 3d-2p mixing between oxygen and transition metal. Owing to the overlap of Fe^{3+}- 3d and 4p states through O 2p states, there is a dipolar nature to this peak, making it generally more intense than pure quadrupolar, pre-edge excitations. The main-edge region which arises from dipolar Fe 1s→4p excitations could be treated in the multiple scattering theoretical framework. In accordance with previous studies [55] and comparison with α-Fe_2O_3 spectrum [56, 57] the first peak centered at around 7115 eV is associated to local excitations of 1s electrons to d levels. This pre-edge do not vary with the Fe content which means that Fe *d* levels are not perturbed by the increasing loading. However, this pre-edge is more intense than that observed for α-Fe_2O_3 with the same Full Width at Half Maximum. It means that the local symmetry differs from the C_{3v} point group of distorted FeO_6 octahedral environment identified for α-Fe_2O_3. Then, Fe^{3+} cations into ceria occupy more non-centrosymmetric sites than in α-Fe_2O_3. ⬚nother feature appears at 7118 eV and results from a delocalized Fe-O-M inter-site hybrid excitation, where M is the first metal site in the coordination sphere of Fe. The intensity of this peak is related (i) to the Fe-O-M bond angle, (ii) the Fe-O bond length and (iii) the coordination number of Fe^{3+}. This peak is slightly more pronounced for the smaller Fe content corresponding to x =0.05 and 0.10 prepared by microwave-assisted solvothermal route which mean that the Fe-O-M interactions change a little bit in this series. However in the white line region corresponding to 1s→4px, 4py, 4pz transitions related to Fe^{3+} anti-bonding orbitals, clear differences can be noticed. The two intense peaks at 7130 eV and 7140 eV are well separated for the lowest Fe concentration and shift one from each other as the Fe content increases. Moreover, for the same Fe rate equal to x=0.10, convolution of both these white lines is observed for the compound prepared by CP process. The comparison of theses edges with α-hematite Fe_2O_3 ones show also clear difference where the white line observed for α-hematite Fe_2O_3 could result from the convolution of two well separated lines identified for $Ce_{1-x}Fe_xO_{2-x/2}$ solid solutions. Furthermore, clear differences appear also on the Fourier Transform of the EX⬚FS oscillations (Fig 8-b), for the first shell associated to Fe-O radial distribution and the second shell related to Fe-Fe(Ce) interactions and multiple scattering phenomena.

Two kinds of Fe-O bond distances appear for α-Fe_2O_3 and $Ce_{0.9}Fe_{0.1}O_{1.95}$ oxide prepared by co-precipitation process where Fe clusters rate seems to be high. This is not the case for $Ce_{0.9}Fe_{0.1}O_{1.95}$ oxide prepared by microwave-assisted solvothermal route where only one but large Fe-O contribution has been identified. The intensity of the second shell for both $Ce_{0.9}Fe_{0.1}O_{1.95}$ oxides is low where the disorder is high compared to α-Fe_2O_3. Then the variation of the X-NES and EX-FS features with the Fe content or the synthesis route can be directly related to the occurrence of Fe-O-Fe interactions and the clusters formation. Then for the MW-assisted route, the Fe cluster rate increases with the Fe concentration and when CP-method is used. Furthermore, these results are in good agreement with the previous EPR and Mössbauer investigations. Moreover these Fe K-edge X-NES spectra exhibit some similarities with those of doped Fe zirconia-ceria solid solution [58] or Fe-promoted sulphated zirconia samples [59]. Then, Fe cluster and isolated Fe^{3+} in distorted octahedral site can be also stabilized in Zr-based compounds.

Finally, The EX-FS spectra recorded at room temperature of the $Ce_{1-x}Fe_xO_{2-x/2}$ solid solution prepared by MW-assisted route have been refined. EX-FS oscillations appear up to 10 $Å^{-1}$. On the Fourier transform, only the first shell corresponding to Fe-O bond distance has been refined and no further shells can be detected because of the low signal/noise ratio (Figure S1-supporting information, Table 3). Then six oxygen neighbors with an average radial bond distance around 1.98 Å and a high Debye-Waller factor around 0.01 $Å^2$ associated mainly to static disorder have been refined. These values are in good agreement with the previous analysis using various spectroscopies. However, the very short average Fe-O radial distance which is fairly compatible with Fe^{3+}, is strongly different from Ce-O ones at 2.33 Å in Fe-doped ceria. Then, major constrains into fluorite network have to considered with a highly static disorder of Fe^{3+} ions randomly distributed into ceria.

(c) Discussion about the occurrence of isolated Fe^{3+} ions and Fe clusters stabilized into ceria network

On the basis of these features and the occurrence of Fe^{3+} stabilized in clusters and isolated octahedral sites, an interpretation of the cell parameter variation and the solubility limit for both the synthesis route can be given. The MW-assisted route allows getting the higher concentration of Fe^{3+} isolated octahedral site, randomly distributed

into the fluorite network. Each oxygen atoms and anionic vacancies occupy a tetrahedral site with a random distribution of Ce^{4+} and Fe^{3+} ions on each vertex. Then, by considering a binomial law, various proportions of OCe_4, $OFeCe_3$ associated to isolated Fe^{3+} cations, OFe_2Ce_2 and OFe_3Ce local environments related to Fe^{3+} clusters, can be estimated as a function of x Fe rate. The rate of each site versus x Fe content has been represented on Figure S2 (Supporting information) on the basis of a binomial law:

$$C_n^k = \frac{n!}{k!\,(n-k)!}\,\binom{n}{k}\,p^k q^{(n-k)}$$

The larger variation of the cell parameter for compounds prepared by MW-assisted route (Figure 2) can be associated to the higher content of isolated Fe^{3+} rate which contribute to create smaller distorted environments stabilized with oxygen vacancies and affect the global network. For the Fe cluster environment, the reorganization of oxygen and vacancies around Ce^{4+} do not have the same impact on the cell parameter and only the local environment of Ce^{4+}, close to the Fe cluster, will be affected. Then a few portion of Ce^{4+}-O^{2-} bond lengths decreases in the case of Fe^{3+} cluster and contribute to a lower reduction of the cell parameter than in the case of isolated Fe^{3+} ion. By comparing the variations of the cell parameter for both these synthesis routes (Figure 2), a big change seems to occur at x=0.07 when the $OFeCe_3$ and OFe_2Ce_2 environments become non-negligible, around 22,5% and 2,6% respectively on the basis of a binomial law. At x=0.15, the $OFeCe_3$ environment rate around 37% brings near again the OCe_4 site proportion (52%) where the OFe_2Ce_2 and OFe_3Ce total content is around 11%. Beyond this Fe rate (x=0.15), the proportion of isolated Fe sites is probably too high with too much constrains on the fluorite-type network for the compounds prepared by MW-assisted route. At x=0.20, the proportion of OCe_4 and $OFeCe_3$ sites are equal (41%) and the $OFeCe_3$ local environment content reaches a maximum at x=0.25 (42%) beyond the limit of solubility of the $Ce_{1-x}Fe_xO_{2-x/2}$ solid solution prepared by CP-process. Thus, too much constrains appear at x=0.25, even with the larger concentration of Fe cluster in the case of compounds prepared by CP method. On the chemistry point of view, the fast microwave-assisted hydrothermal route helps to the formation of a large proportion of isolated Fe^{3+} randomly distributed around Ce^{4+} ions. With the CP process followed by annealing at T=600°C, a major proportion of Fe^{3+} clusters can be identified. Then, during the synthesis, a competition occurs between the affinity of Fe^{3+} for Ce^{3+}/Ce^{4+} ions because of their electronegativity difference and the capability of Fe^{3+} to create Fe-

O-Fe bonds. Finally, one should have to note that the two isolated Fe^{3+} distorted octahedral sites can be found in Bixbyite $(Fe,Mn)O_3$ whose the structure derive from the fluorite-type network.

(d) Reducibility properties.

Thermogravimetric analyses were carried out under reducing atmosphere ($\Box r/5\%H_2$) up to 700 °C (Figure 9). When the slope of the curves change drastically for the Fe-substituted ceria, one can consider in a first approximation that mainly, the reductions of Fe^{3+} and Ce^{4+} occur simultaneously with the oxygen loss from the fluorite-type network. Several compounds synthesized using CP and MW-assisted routes were analyzed. Whatever the compositions, the incorporation of iron into ceria enhances the reducibility (or the amount of reduced cations) of these compounds for both syntheses routes with a decrease of temperatures corresponding to the first reduction between T=300°C and T=400°C. Taking into account the molar mass of the $Ce_{1-x}Fe_xO_{2-x/2}$ solid solution, a weight loss equal to 1% corresponds to 0.1 Oxygen moles departure associated to 0.2 moles of reduced Ce^{4+}/Fe^{3+} with the formation of 0.2 moles of Ce^{3+}/Fe^{2+}. The reduction process of this solid solution – leading to stabilization of metallic iron – will be described in a forthcoming paper. $\Box$ maximum of weight loss at T=400°C and T=700°C is reached for low Fe content around x=0.05 corresponding to MW-assisted compounds whereas a gradual decrease of weight loss at T=400°C and T=700°C versus x Fe rate can be noted for CP- compounds. For MW-assisted compounds, as previously shown, the rate of Fe^{3+} stabilized in isolated distorted octahedral sites remains high for low Fe content and the impact on Ce^{4+} first neighbors with distorted environments and their reduction rate will be high and reach a maximum for low Fe content. This maximum is around x=0.05-0.07. Moreover the occurrence of nano-cubes with {001} faces for low Fe rate should also explain the better reducibility of these compounds. The competition between the formation of nano-polyhedra with less exposed {001} planes and the higher surface areas as the Fe rate increases, tend also to stabilize the content of reduced species as the Fe amount increases starting at x > 0.05. For instance, the MW-assisted CeO_2 and $Ce_{0.95}Fe_{0.05}O_{1.97}$ compounds with cubic shapes and comparable surface areas exhibit 30% and 60% reducibility rates (Ce^{4+}/Fe^{3+} ions reduced into Ce^{3+}/Fe^{2+} ones) respectively (1.5% and 3% weight losses associated to oxygen departure respectively) at T= 550°C. Then, just a 5% doping of a major

quantity of isolated Fe^{3+} into ceria contribute to double the reducibility rate of these materials prepared by MW-assisted route. The larger proportion of isolated Fe^{3+} ions stabilized into ceria contribute to create more ionic bonds around Ce^{4+}/Fe^{3+} with a higher oxygen mobility than in the case of Fe^{3+} clusters where the covalency of the metal-oxygen bond around Fe^{3+} increases. Consequently, the reduction rate is larger as the proportion of isolated Fe^{3+} ions into ceria increases. Beyond x=0.05-0.07, the proportion of isolated Fe^{3+} remains high but do not strongly change and the reducibility properties are almost the same whatever the x Fe content. Furthermore, one should have to notice that compounds with a lower Ce amount and a higher Fe rate (x=0.15), exhibit also the maximum reduction rate which appears at lower temperature around T=300°C. In this temperature range, a forthcoming paper [60] will show that Ce^{4+} and Fe^{3+} ions are simultaneously reduced.

As far as the $Ce_{1-x}Fe_xO_{2-x/2}$ solid solution prepared by CP method followed by annealing at T= 600°C is concerned, because the proportion of Fe^{3+} clusters is dominant with this synthesis route, fewer Ce^{4+} are affected by Fe^{3+} local distortions. Furthermore, the oxygen mobility and the reduction of metallic cations when Fe clusters are the dominant species, are lower because of the reorganization of the oxygen network around Ce^{4+} and the location of oxygen vacancies around Fe clusters. A higher Fe content is necessary for this synthesis route in order to reach a high Fe clusters content which can affect a maximum of Ce^{4+} reduced ions. Then, as the Fe content rises, a gradual increase of reduction rate is observed due to the progressive distribution of Fe clusters into ceria with this synthesis route. For x=0.15, the weight loss is around 2% at T=550°C with an approximated reducibility rate of 40% (Ce^{4+}/Fe^{3+} ions reduced into Ce^{3+}/Fe^{2+} ones).

Conclusions

In order to prepare the $Ce_{1-x}Fe_xO_{2-x/2}$ solid solution, two various routes have been used: the classical co-precipitation of Ce^{3+} and Fe^{3+} nitrates at room temperature in basic medium (2h maturation) followed by annealing at T=600°C under air (5h) and the unusual microwave-assisted hydrothermal synthesis of Ce^{3+} and Fe^{3+} nitrates in basic medium at T=200°C (40 min). In these last conditions, kinetics effects occur and metastable phases can be stabilized. XRD, TEM and BET experiments show clear

differences for both these synthesis routes. For the compounds obtained by microwave-assisted route, the solubility limit of Fe^{3+} into ceria is smaller (x=0.15 against x=0.20 for CP-method) but the amplitude of cell parameter variation is larger. With this synthesis route, nano-cubic morphologies are obtained for low Fe^{3+} content and nano-polyhedra are stabilized for larger Fe^{3+} amount with higher surface areas. The local Fe^{3+} environments analyzed by EPR, Mossbauer and X⬚NES-EX⬚FS spectroscopies, depend also on the synthesis route and a higher content of isolated Fe^{3+} can be identified for compounds prepared by MW-assisted route in good agreement with the larger variation of the cell parameter determined by XRD. Such isolated Fe^{3+} stabilized in distorted octahedral sites with orthorhombic and axial distortions can be identified in $(Fe,Mn)O_3$ bixbyite-type structure [46] which corresponds to a superstructure of the fluorite-type network. On the basis of a binomial law and a distribution of OM_4 tetrahedra into fluorite-type network, it is interesting to note that the OFe_2Ce_2 (Fe^{3+} cluster) and $OFeCe_3$ (isolated Fe^{3+} ions) sites proportions become non-negligible around 2% and 22% respectively for x=0.07. It is also interesting to mention at this Fe (x) rate, the surface areas change drastically for both these synthesis routes. Moreover, the distribution of OM_4 tetrahedra on the basis of a binomial law, shows when the proportions of OCe_4 and $OFeCe_3$ sites become near or equal with a rate of OFe_2Ce_2 superior to 10%, the solubility limits of x=0.15 (MW-assisted process) and x=0.20 (CP method) are reached. Thus, too much constrains appear around Ce^{4+} for these Fe concentrations and lead to the formation of α-hematite Fe_2O_3. ⬚s far as the reducibility properties are concerned, a maximum of reduction rate is reached for low Fe content (x=0.05) and compounds prepared by MW-assisted route. The first reduction phenomena occurs between T=300°C and T=400°C with a concomitant redox process involving Ce^{4+} and Fe^{3+} which will be discussed in a forthcoming paper [60]. Moreover, the reduction rate at T=550°C increases drastically from 30 % (without Fe) to 60% (5% mol Fe). The same reduction rates for higher Fe contents can be explained by different effects associated to the local impact of isolated Fe^{3+} ions on Ce^{4+} nearest neighbors but also to the morphology and surface area changes versus x Fe content. Finally, for compounds prepared by the classical CP-process, the gradual increase of reduction rate up to x= 0.20 (limit of solubility) can be related to the progressive stabilization of Fe clusters which affect regularly the Ce^{4+} nearest neighbors. Furthermore, the ionic conductivity of Fe-substituted ceria will be strongly affected by the distribution of isolated Fe^{3+} cations and

Fe^{3+} clusters into fluorite network. This description with isolated polarizing cations and clusters stabilized into ceria or derived fluorite network can be extended to other transition metals such as Mn and Ti. Furthermore, the stabilization of such local environments will strongly affect the reactivity and the redox properties (Automotive Exhaust Catalysts and Photocatalysis) as well as the ionic conductivity (Solid Oxide Fuel Cell)) or the magnetic interactions (Spintronic applications).

Supporting information:

Figure S1 showing experimental and fitted Fourier transforms for k^3-weighted Fe K-edge EXAFS spectra of $Ce_{1-x}Fe_xO_{2-\delta}$ compounds with a) x = 0.05, b) 0.1, c) 0.15 and d) 0.17 (recorded at room temperature), **Figure S2** showing proportion of $OCe_{4-n}(Fe)_n$ tetrahedral (n integer, $0 \leq n < 4$) versus x Fe content determined on the basis of a binomial law (C_n^p).

Acknowledgements

REFERENCES

[1] Funabiki, M.; Yamada, T.; Kayano, K. *Catal. Today* **1991**, *10*, 33

[2] Trovarelli, A. *Catalysis by ceria and related materials*, Imperial College Press, **2002**

[3] Singh, P.; Hedge, M.S. *Mater. Lett.* **2008**, *181*, 3248

[4] Reddy, B.M.; Reddy, G.K.; Ganesh, I.; Ferreira, J.M.F. *Catal. Lett.* **2009**, *130*, 227

[5] Achary, S.N.; Kali, S.K.; Kulkarni, N.K.; Krishna, P.S.R.; Shinde, A.B.; Tyagi, A.K. *Chem. Mater.* **2009**, *21*, 5848.

[6] Bueno-Lopez, A.; Krishna, K.; Makkee, M.; Moulijn, *J. Catal.***2005**, *230*, 237

[7] McBride, J.R.; Hass, K.C.; Poindexter, B.D.; Weber, W.H. *J. Appl. Phys.***1994**, *76*, 2435

[8] Li, J-G.; Ikegami, T.; Mori, T.; Wada, T. *Chem. Mater.***2001**, *78*, 433

[9] Yahiro, H.; Eguchi, Y.; Eguchi, K.; Arai, H. *J. App. Electrochem.***1988**, *18*, 527

[10] Hernandez, W.Y.; Centeno, M.A.; Romero-Sarria, F.; Odriozola, J.A. *J. Phys. Chem. C,***2009**, *113*, 5629

[11] Wang, F-Y.; Chen, S.; Cheng, S. *Electrochem. Commun.* **2004**, *6*, 743

[12] Hungria, A.B.; Martinez-Arias, A.; Fernandez-Garcia, M.; Juez, A.I.; Guerrerro-Luiz, A.; Calvino, J.J.; Conesa, J.C.: Soria, *J. Chem. Mater.,* **2003**, *15*, 4309.

[13] Yoshima, M ; Hirose, T; Katano, S; Suzuki, T; Kakihana, M ; Yoshimura, M *Phys. Rev. B*, 51, **1995**, 8434-8437.,

[14] Kuemmerle, K.A ; Heger, G *J. Sol. Stat. Chem*, 147, **1999**, 485-500

[15] Florea, I.; Feral-Martin, C.; Majimel, J.; Ihiawakrim, D.; Hirlimann, C.; Ersen, O. *Cryst. Growth & Design*, **2013**,13, 1110-1121

[16] Si. R, Flytzani-Stephanopoulos, Angew. Chem. Int. Ed, 47,2008, 2884-2887.

[17] Pérez-Alonso, F.; Lopes Granado, M.; Ojeda, M.; Terreros, P.; Rojas, S.; Herranz, T.; Fierro, J.L.G.; *Chem. Mater.,* **2005**, *17*, 2329

[18] Li, K.; Wang, H.; Wei, Y.; Yan, D. *Appl. Catal. B environ.* **2010**, *97*, 361

[19] Laguna, O.H.; Centeno, M.A.; Arzamendi, G.; Gandia, L.M.; Romano-Sarria, F.; Odriozola, J.A. *Catal. Today* **2010**, *157*, 150

[20] Li, K.Z.; Wang, H.; Wei, Y.G. *J. Phys. Chem. C,* **2009**, *113*, 15288

[21] Thomson. J.B, Armstrong. A.R, Bruce. P.G, *J. Am. Chem. Soc*, 118, **1996**, 11129-11133

[22] Tolla. B, Demourgues. A, Isnard. O, Menetrier. M, Pouchard. M, Rabardel. L, Seguelong. T, J. *Mater. Chem,* 9, **1999**, 3131-3136.

[23] Yue, L.; Zhang, X-M.; *J. Alloy Compd,* **2009**, *475*, 702

[24] Dutta. G, Waghmare. U.V, Baidya. T, Hedge. M.S, Priolkar. K.R, Sarode. P.R, *Chem. Mater*, 18, **2006**,3249-3256

[25] Li, X.; Wei, S.; Zhang, Z.; Zhang, Y.; Su, Q.; Gao, X. *Catal. Today***2011**, *175*, 112

[26] Quaino, P.; Sysgantseva, O.; Siffert, L.; Tielens, F.; Minot, C.; Calatayud, M. *Chem. Phys. Lett.***2012**, *519*, 69

[27] Yabe, S.; Sato, T. *J. Sol. State Chem.***2003**, *171*, 7

[28] Lv, H.; Tu, H.; Zhao, B.; Wu, Y.; Hu, K. *Solid State Ionics***2007**, *177*, 3467

[29] Kaneko, H.; Ishihara, H.; Taku, S.; Naganuma, Y.; Hasgawa, N.; Tamaura, Y. *J. Mater. Sci.* **2008**, *43*, 3153

[30] Li, K.; Wang, H.; Wei, Y.; Liu, M. *J. Rare Earth* **2008**, *26*, 245

[31] Aneggi, E.; de Leitenburg, C.; Dolcetti, G.; Trovarelli, A. *Catal. Today* **2006**, *114*, 40

[32] Gupta, A.; Kumar, A. *Chem. Mater.* **2009**, *21*, 4880

[33] Bao, H.; Chen, X.; Fang, J.; Jiang, Z.; Huang, W. *Catal. Commun.* **2008**, *125*, 160

[34] Kaminura, Y.; Sato, S.; Takahashi, R.; Sodesawa, T.; Akashi, T. Appl. *Catal. A: Gen.* **2003**, *252*, 399.

[35] Li, G, Smith. R.L, Inomata. H, *J. Am. Chem. Soc.* . **2001**, *123*, 11091.

[36] Singh. P, Hedge. M.S, *Dalton Trans*, 39, **2010**, 10768-10780.

[37] Dohcevic-Mitrovic. Z.D, Paunovic. N, Radovic. M, Popovic. Z.V, Matovic. B, Cekic. B, Ivanovski. V. *App. Phys. Lett* 96, **2010**, 203104.

[38] Matovic. B, Dohcevic-Mitrovic. Z, Radovic, Brankovic. Z, Brankovic. G, Boskovic. S, M, Popovic. Z.V, *J Pow. Sources*, 193, **2009**, 146-149.

[39] Michael, D.; Mingos, P.; Baghust, D.R. *Chem. Soc. Rev.* **1997**, *26*, 233

[40]. Rodriguez-Carvajal, J. Physica B.(1993),192,55

[41] C. Prestipino, O. Mathon, R. Hino, A. Beteva and S. Pascarelli, *J. Synchrotron Rad.* (2011). **18**, 176-182.

[42] S Belin, V. Briois, A. Traverse, M. Idir, T. Moreno, M. Ribbens 2005 *Phys.Scr.* **2005** 980.

[43] M. Newville, *J. Synchrotron Rad.* **8**, pp 322--324 (2001)

[44] Thompson. P, Cox. D.E, Hastings. J.B, J. Appl. Crystallography, 1987, 20, 79.

[45] Hernandez, W.Y.; Centeno, M.A.; Romero-Sarria, F.; Odriozola, J.A. *J. Phys. Chem. C* **2009**, *113*, 5629

[46] Sronek, L.; Majimel, J.; Kihn, Y.; Montardi, Y.; A. Tressaud; C. Feist; M. and Legein; Buzaré, J.-Y.; Body, M.; Demourgues, A. *Chem. Mater.* **2007**, *19*, 5110

[47] Guodong, F.; Changgen, F.; Zhao, Z. J. Rare Earth 2007, 25, 42

[48] Hernandez, W.Y.; Laguna, O.H.; Centeno, M.A.; Odriozola, J.A. *J. Solid. State Chem.* **2011**, *184*, 3014

[49] Kumar Singh, R.; Srinivasan, A.; *J. Magnet. Magnet. Mat.* **2010**, *322*, 2018

[50] Sreekanth Chakradhar, R.P.; Sivaramaiah, G.; Lakshmana Rao, J.; Gopal, N.O. *Spectrochim. Acta A* **2005**, *62*, 51

[51] Geller. B, *Acta. Cryst. B*, **1971**, 27, 821-828

[52] Zhilinskaya, E.A.; Lazukin, V.N.; Bychkov, E.A. and Likholit, I.L. *Journal of Non-Crystalline Solids* **1990**, 119, 263.

[53] Martinez-Arias, A.; Coronado, J.M.; Conesa, J.C. and Soria, J. in: *Rare Earths*, eds. R. Sáez Puche and P. Caro (Complutense, Madrid, 1997) p. 299.

 [54] Abi-aad, E.; Bechara, R.; Grimblot, J. and Aboukaïs, A. *Chem. Mater.* **1993**, *5*, 793-797.

[55] Sigrist. J.A, Gaultois. M.G, Grosvenor. A.P, *J.Phys.Chem A,* **2011**, 115, 1908-1912

[56] Caliebe, W. A.; Kao, C.-C.; Hastings, J. B.; Taguchi, M.; Kotani, A.; Uozumi, T.; Groot, F. M. F. de . Phys. Rev. B 1998, 58, 13452–13458.

[57] Glatzel, P.; Mirone, A.; Eeckhout, S. G.; Sikora, M.; Giuli, G. Phys. Rev. B 2008, 77, 115133.

[58] Mastelaro, V.R.; Briois, V.; de Souza, D.P.F.; Silva, C.L. *J. Eur. Ceram. Soc.* **2003,** 23, 273

[59] Yamamora, T.; Tanaka, T.; Tanekaka, T.; Yoshida, S.; Onari, T.; Takahashi, Y.; Kosaka, T.; Hasgawa, S. *J. Synchrotron Radiat.***1999**, *6*, 425

[60] Moog. I, Prestipino. C, Figueroa. S, Majimel. J and Demourgues. A. Accepted in J. Phys. Chem C.

Compositions	Lattice parameter (Å)	Crystallite size (nm)	Surface area (m^2/g)
CeO_2 (MW)	5.413(1)	19(2)	40(4)
CeO_2 (CP)	5.411(1)	20(2)	23(3)
$Ce_{0.98}Fe_{0.02}O_{1.99}$ (MW)	5.408(1)	18(2)	44(5)
$Ce_{0.98}Fe_{0.02}O_{1.99}$ (CP)	5.403(1)	9(1)	32(4)
$Ce_{0.95}Fe_{0.05}O_{1.98}$ (MW)	5.400(1)	14(2)	58(6)
$Ce_{0.95}Fe_{0.05}O_{1.98}$ (CP)	5.398(2)	9(1)	71(7)
$Ce_{0.93}Fe_{0.07}O_{1.97}$ (MW)	5.392(2)	10(2)	90(9)
$Ce_{0.93}Fe_{0.07}O_{1.97}$ (CP)	5.400(2)	14(2)	40(4)
$Ce_{0.9}Fe_{0.1}O_{1.95}$ (MW)	5.384(2)	9(1)	91(9)
$Ce_{0.9}Fe_{0.1}O_{1.95}$ (CP)	5.394(2)	8(1)	58(6)
$Ce_{0.85}Fe_{0.15}O_{1.93}$ (MW)	5.371(7)	9(1)	95(10)
$Ce_{0.85}Fe_{0.15}O_{1.93}$ (CP)	5.389(3)	9(1)	-
$Ce_{0.83}Fe_{0.17}O_{1.92}$ (MW)	5.367(3)	9(1)	-
$Ce_{0.83}Fe_{0.17}O_{1.92}$ (CP)	5.391(3)	9(1)	47(5)

Table 1: Refined lattice parameters and crystallite sizes using the Fullprof software for the as-prepared compounds. Surface areas determined by BET method are also quoted.

Compositions	DIS	δ (mm/s)	Γ (mm/s)	Δ (mm/s)	Relative abundance %
$Ce_{0.9}Fe_{0.1}O_{1.95}$ (MW)	D1	0.33(1)	0.30	1.23(1)	21±3
	D2	0.38(1)	0.30	0.83(1)	79±3
$Ce_{0.9}Fe_{0.1}O_{1.95}$ (CP)	D1	0.30(1)	0.30	1.17(1)	47±3
	D2	0.37(1)	0.30	0.99(1)	53±3

Table 2: Refined Mössbauer parameters for as prepared compounds : δ: isomer shift; Γ: Full Width at Half Maximum ; Δ : average quadrupole splitting on the basis of a distribution and relative abundance for each components D1 and D2.

Compositions	Coordination number	Radial Distance (Å)	DW factor ($Å^2$)
$Ce_{0.95}Fe_{0.05}O_{1.98}$	6	1.984+/-0.007	0.0091+/-0.002
$Ce_{0.9}Fe_{0.1}O_{1.95}$	6	1.980+/-0.005	0.0086+/-0.001
$Ce_{0.85}Fe_{0.15}O_{1.93}$	6	1.975+/-0.005	0.0081+/-0.001
$Ce_{0.83}Fe_{0.17}O_{1.92}$	6	1.977+/-0.006	0.0091+/-0.001
Common ΔE-zero energy shift -1.54 +/- 0.80			

Table 3: Room temperature EXAFS analysis of the first shell (Fe K-edge) for compounds prepared by MW-assisted route. The coordination number has been fixed to 6 on the basis of previous analyses by Mossbauer and EPR spectroscopies. The zero energy shift, the Fe-O radial bond distance and the Debye-Waller factor (DW) have been refined.
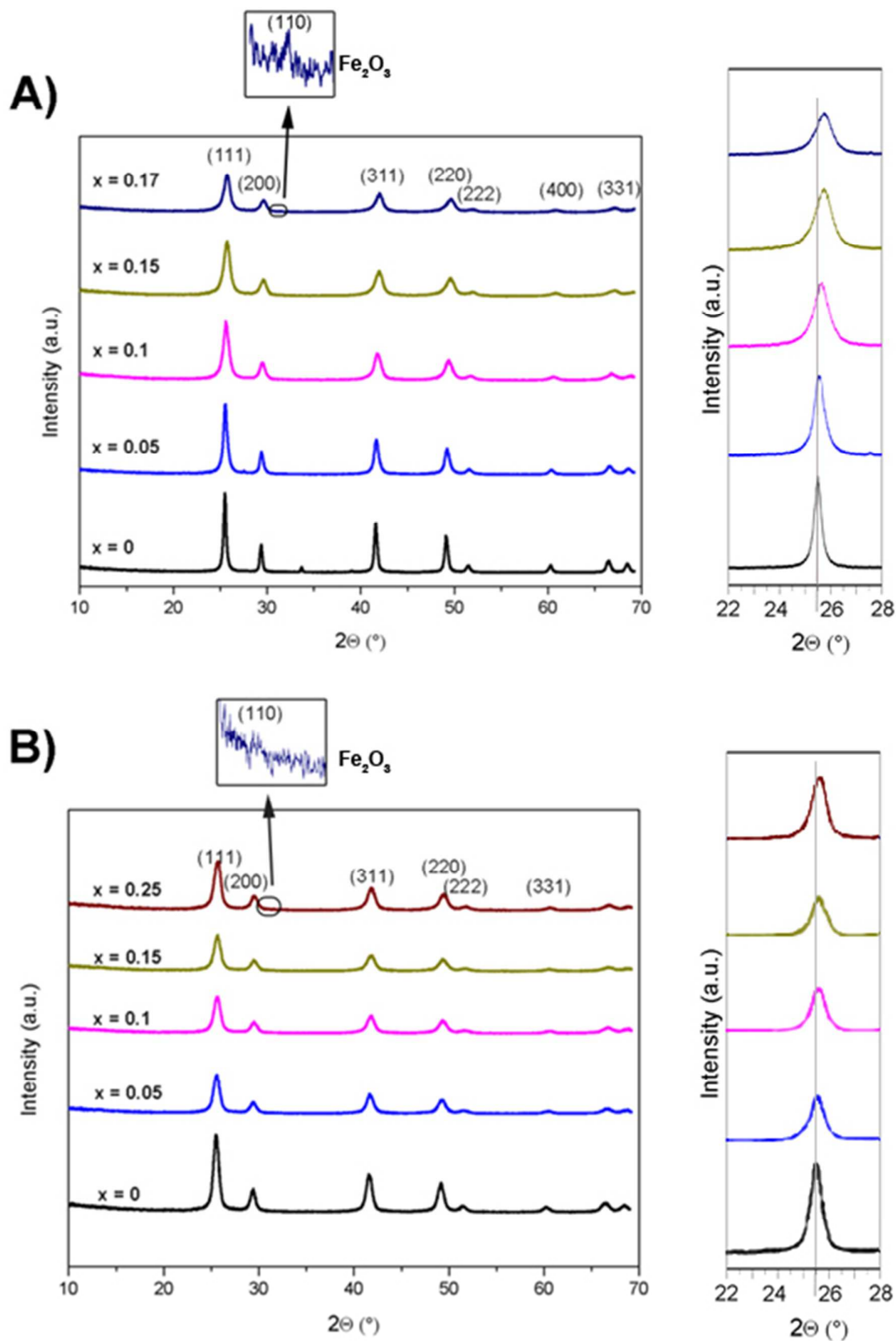
Figure 1: XRD patterns of the $Ce_{1-x}Fe_xO_{2-x/2}$ solid solution prepared by microwave-assisted route (A) and co-precipitation synthesis (B).
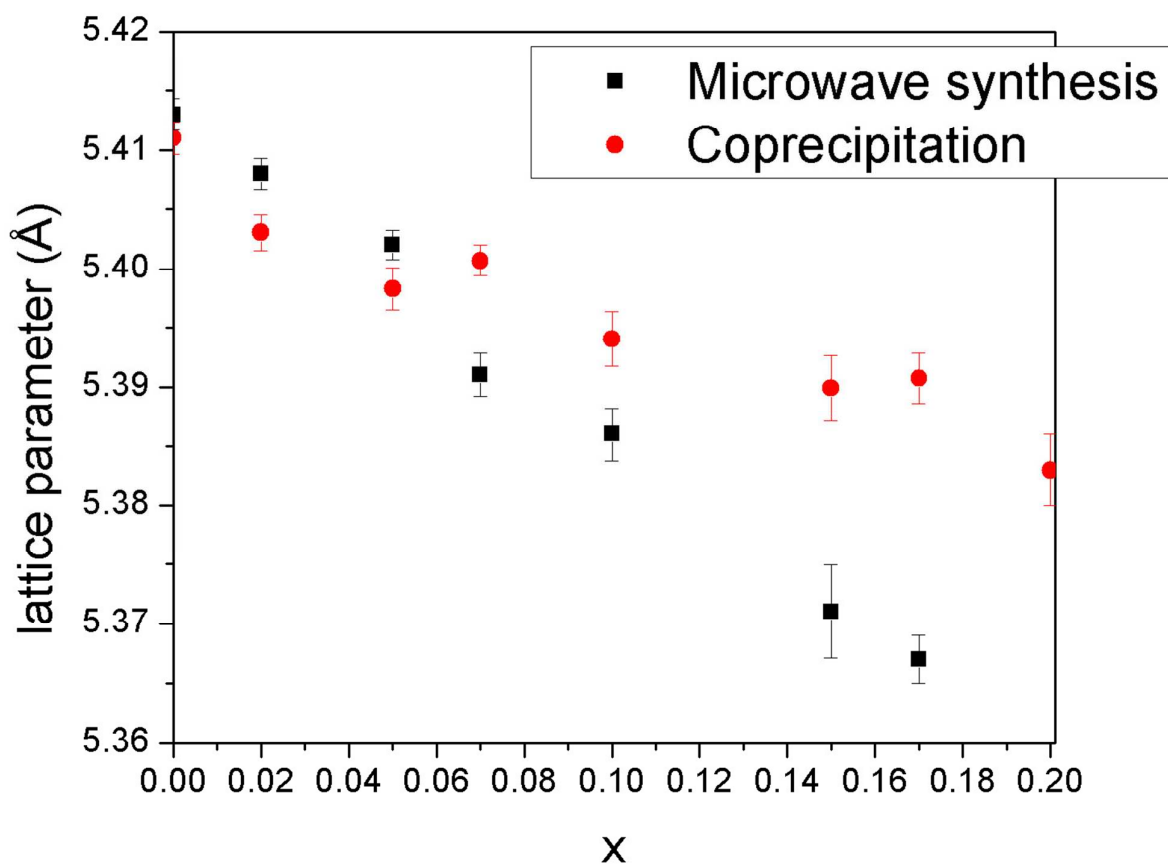
Figure 2 : Variation of the lattice parameter (Full pattern Profile Matching) versus Fe (x) content for as–prepared $Ce_{1-x}Fe_xO_{2-x/2}$ compounds using both synthesis routes.
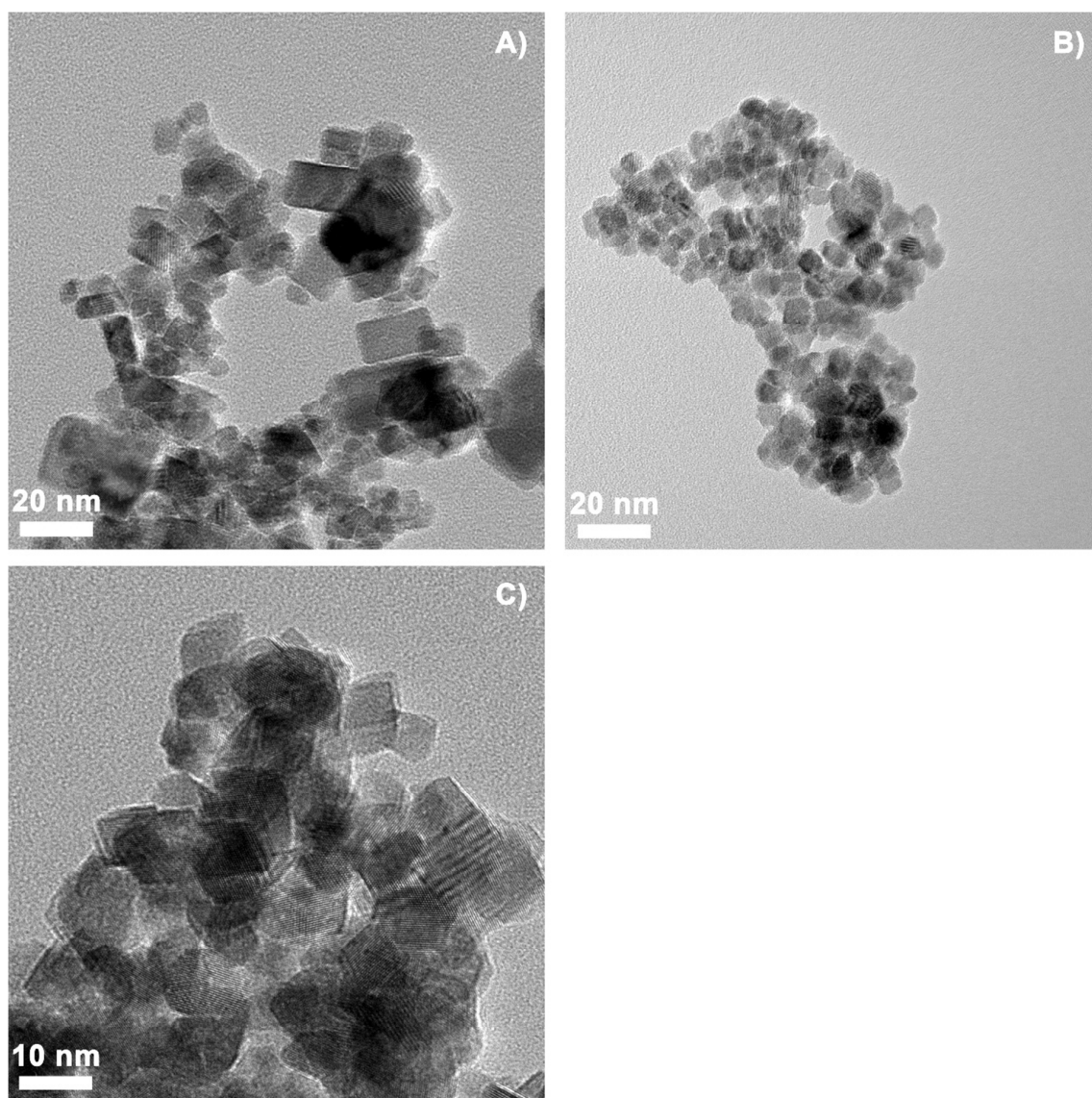
Figure 3: HRTEM micrographs of MW nano-cubes (5% and 15% Fe content, A and B respectively) and CP nano-polyhedra, (15% Fe content, C)
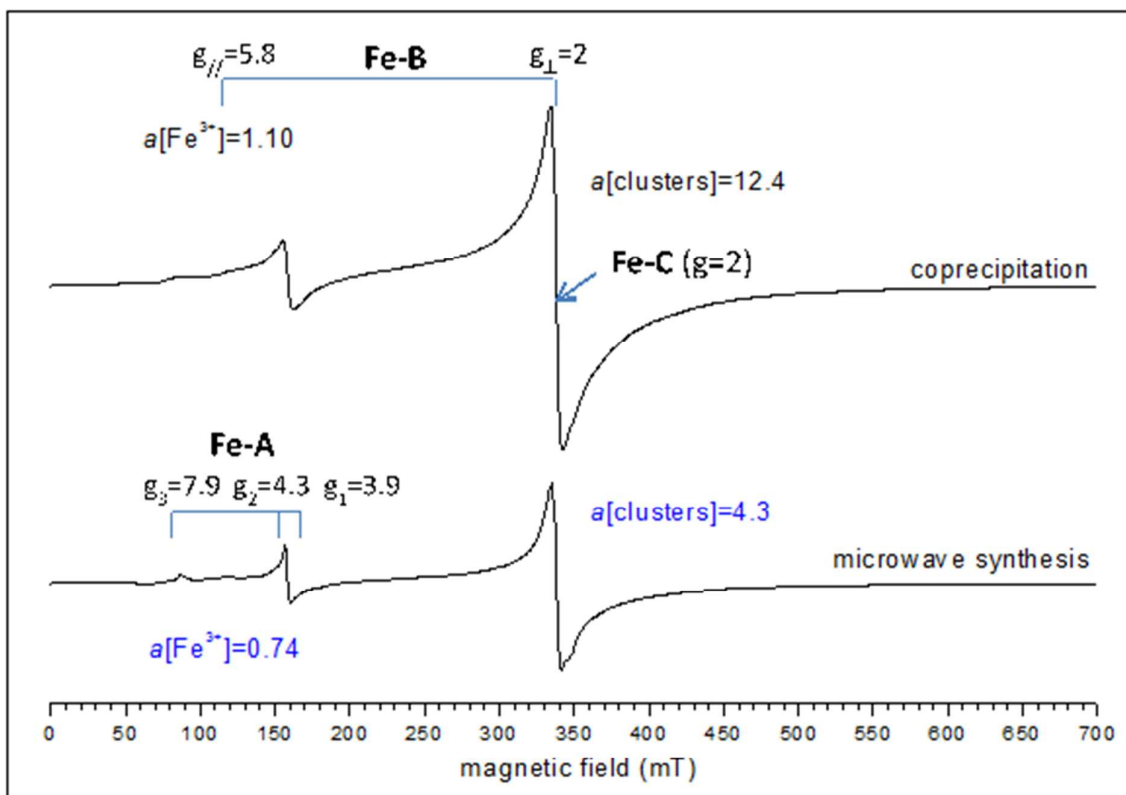
Figure 4: Experimental X-band EPR spectra recorded at 5K of $Ce_{0.9975}Fe_{0.0025}O_{2-\delta}$ compounds prepared by both these synthesis routes (microwave frequency ν = 9.45 GHz, microwaves power P = 10 mW, amplitude of magnetic field modulation MA = 0.6 mT, modulation frequency MF = 100 kHz, spectral resolution SR = 0.5 mT/pt). The a[Fe^{3+} or clusters] integrated area of each zones corresponding to Fe^{3+} isolated ions and Fe clusters are quoted.
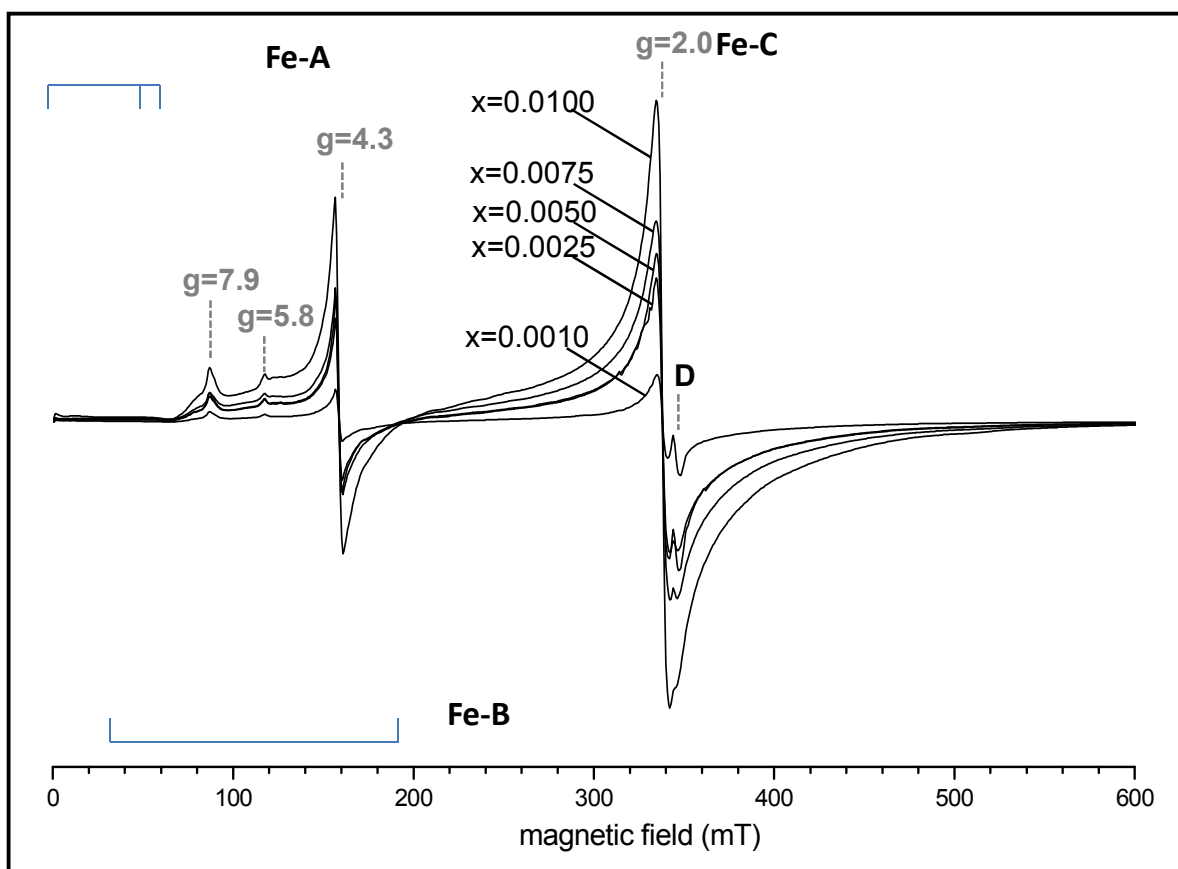
Figure 5: Experimental X-band EPR spectra recorded at T=5K of $Ce_{1-x}Fe_xO_{2-x/2}$ compounds prepared by MW-assisted route for various low Fe x content (0.001<x<0.01).
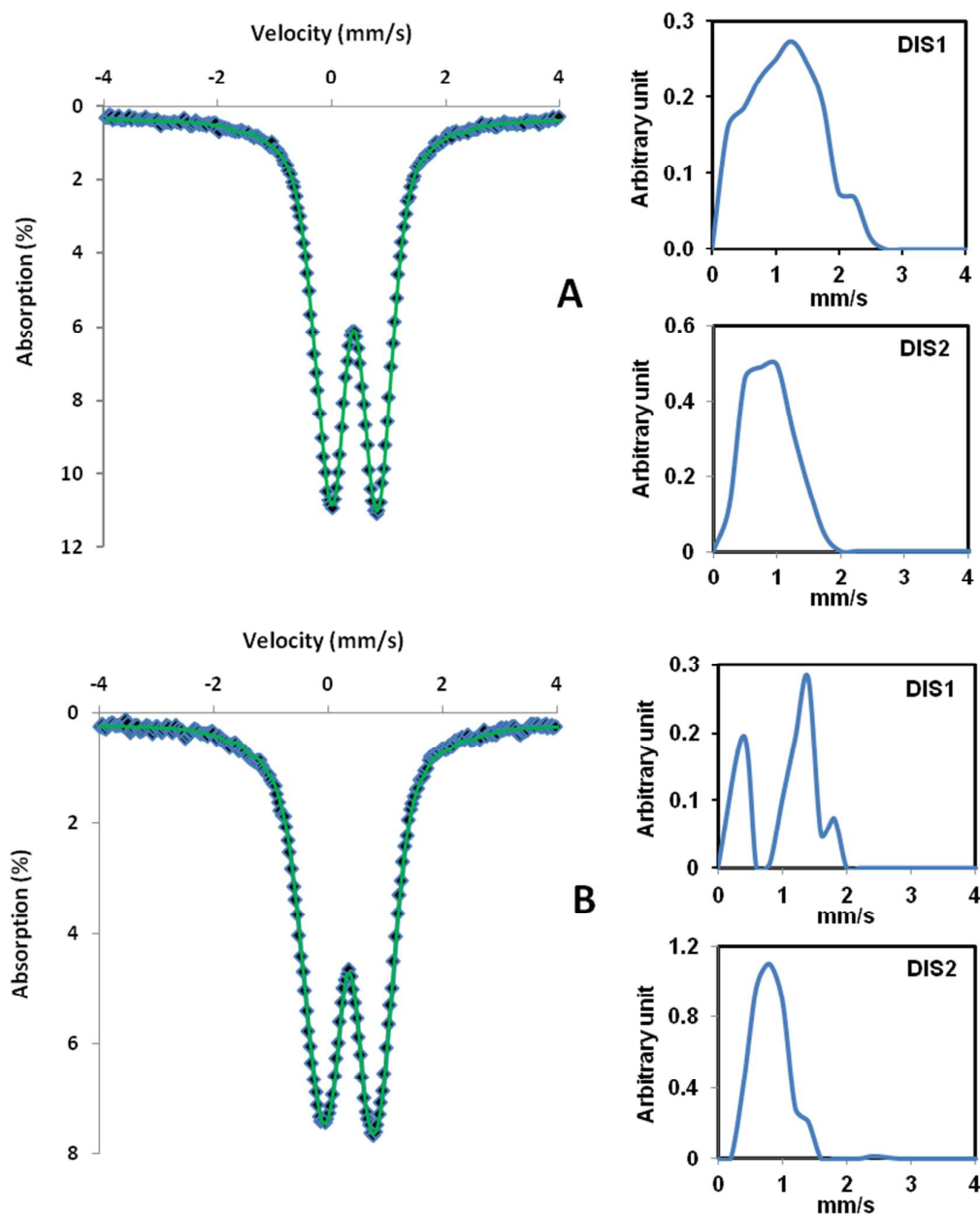
Figure 6: Mössbauer spectra collected at room temperature for $Ce_{0.9}Fe_{0.1}O_{1.95}$ compounds prepared by (A) MW and (B) CP synthesis routes. Dot and solid lines are the experimental and fitted data using the parameters of Table 2 respectively. Distributions of quadrupole splitting for the two sites are shown in the inserts.
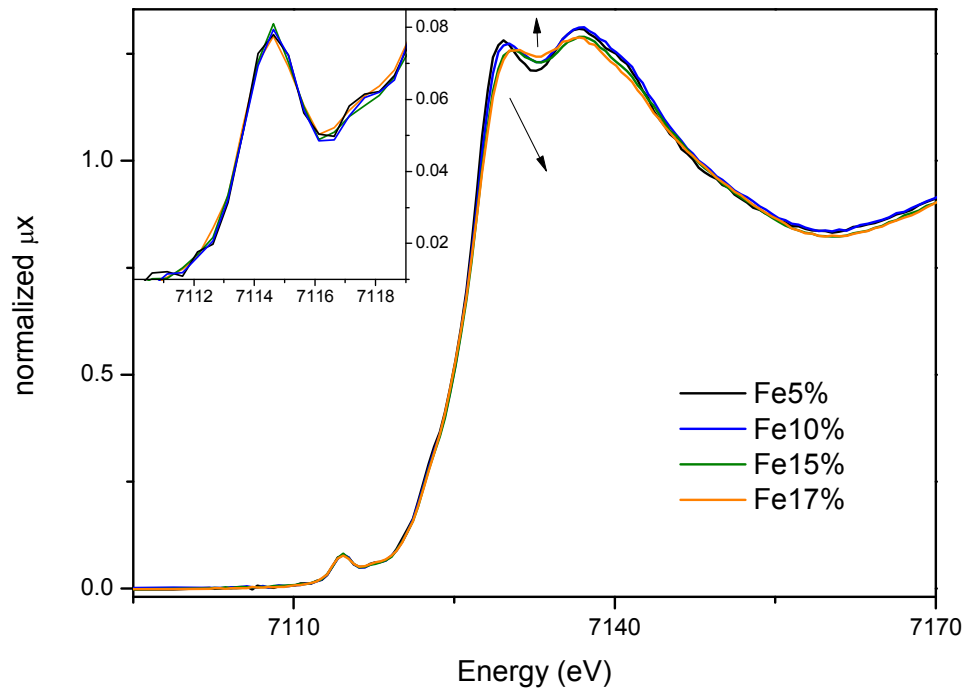
Figure 7: Fe K-edge XANES spectra of $Ce_{1-x}Fe_xO_{2-x/2}$ compounds with x = 0.05, 0.1, 0.15 and 0.17 recorded at room temperature. Insert shows the pre-edge region variation versus x between 7110 eV and 7120 eV.
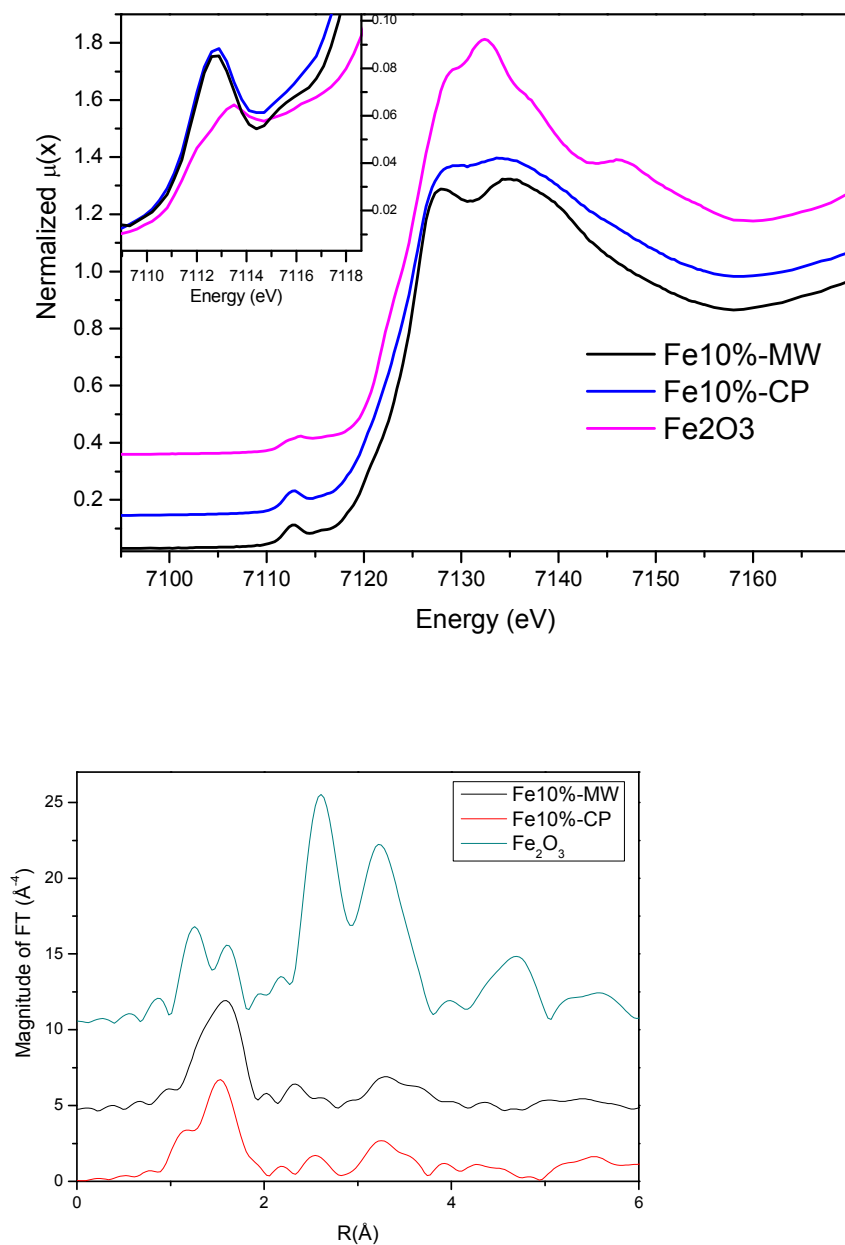
Figure 8 : Fe K-edge XANES spectra (a, above) and Fourier Transforms of EXAFS oscillations (b, below) recorded at T=20K of $Ce_{0.90}Fe_{0.10}O_{1.95}$ compounds (CP and MW-assisted routes) and α-Fe_2O_3 .
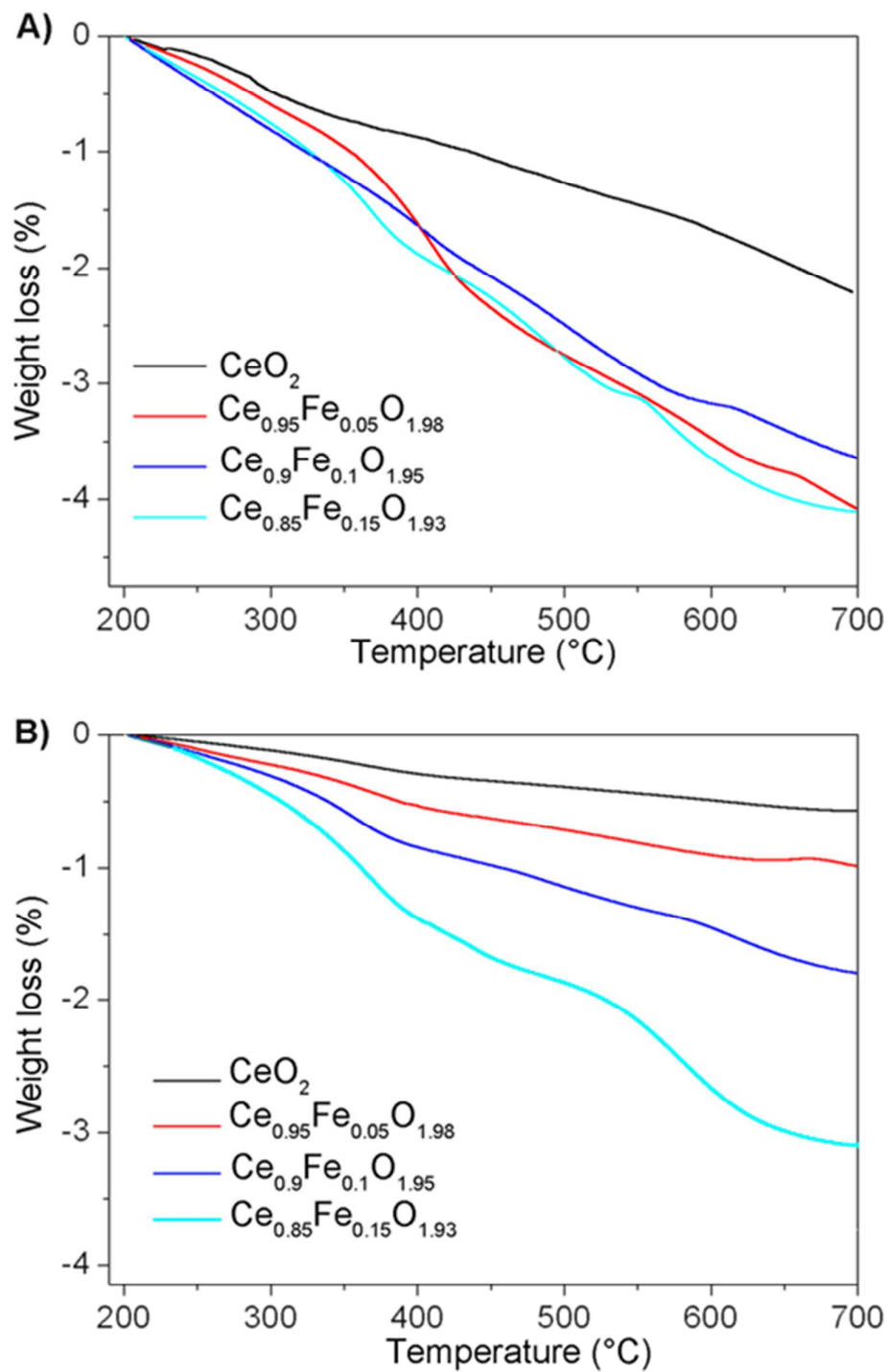
Figure 9: TGA (Ar/5%H₂) of the $Ce_{1-x}Fe_xO_{2-x/2}$ solid solution prepared by microwave-assisted hydrothermal (T=200°C) route (A) and co-precipitation process followed by annealing at T=600°C (B).